This article has been accepted for inclusion in a future issue of this journal. Content is final as presented, with the exception of pagination.

Cluster-Based Empirical Tropospheric Corrections Applied to InSAR Time Series Analysis

Kyle Dennis Murray, Rowena B. Lohman, and David P. S. Bekaert

***Abstract*— Interferometric synthetic aperture radar (InSAR) allows for mapping of crustal deformation on land with high spatial resolution and precision in areas with high signal-to-noise ratios. Efforts to obtain precise displacement time series globally, however, are severely limited by radar path delays within the troposphere. The tropospheric delay is integrated along the full path length between the ground and the satellite, resulting in correlations between the interferometric phase and elevation that can vary dramatically in both space and time. We evaluate the performance of spatially variable, empirical removal of phase-elevation dependence within SAR interferograms through the use of the *K*-means clustering algorithm. We apply this method to both synthetic test data, as well as to C-band Sentinel-1a/b time series acquired over a large area in south-central Mexico along the Pacific coast and inland—an area with a large elevation gradient that is of particular interest to researchers studying tectonic- and anthropogenic-related deformation. We show that the clustering algorithm is able to identify cases where tropospheric properties vary across topographic divides, reducing total root mean square (rms) by an average of 50%, as opposed to a spatially constant phase-elevation correction, which has insignificant error reduction. Our approach also reduces tropospheric noise while preserving test signals in synthetic examples. Finally, we show the average standard deviation of the residuals from the best-fit linear rate decreases from approximately 3 to 1.5 cm, which corresponds to a change in the error on the best-fit linear rate from 0.94 to 0.63 cm/yr.**

***Index Terms*— Interferometric synthetic aperture radar (InSAR), Mexico, slow slip, subduction, synthetic aperture radar (SAR), tropospheric corrections.**

I. Introduction

THE increase in free and open synthetic aperture radar (SAR) data from the recent European Sentinel-1 constellation [1] and the future NASA-ISRO SAR (NISAR) mission provides an unprecedented opportunity to measure how the Earth deforms over time at high spatial resolution (∼5 m) and temporal sampling (6 to 12 days). However, interferometric SAR (InSAR) observations are strongly impacted by path delays caused by refraction within the troposphere, resulting in signals within individual interferograms with magnitudes of up to tens of centimeters. This delay is commonly modeled as the combination of two separate components: the hydrostatic and wet components [2], [3]. The hydrostatic component varies relatively smoothly as a function of pressure and temperature over longer length scales (> 100 km), whereas the wet component is more turbulent—varying rapidly as a function of water vapor and temperature over shorter temporal and spatial scales than the hydrostatic component [4]. Dense temporal sampling allows the impact of tropospheric effects on inversions for quantities such as the average secular rate to be diminished by means of temporal averaging [5], [6]. However, relying on temporal averaging is not sufficient for many research targets, particularly those that rely on data from older satellites with low temporal resolution, as well as for the study of many tectonic and anthropogenic-related processes that vary over short timescales. Independent data sets, such as weather reanalysis models [7], spectrometer data [8], and GPS zenith total delays [3], are often used to estimate and subtract troposphere-derived signals from interferograms. These approaches, however, have shown highly variable degrees of success and are sensitive to gaps in time between the independent data and the SAR acquisitions [9]–[11]. Empirical approaches that leverage assumptions about the spatial or temporal characteristics of the tropospheric component of the phase or the displacement signal itself can be used in cases where independent constraints on tropospheric properties are unavailable or are expected to be unreliable (e.g., regions with rapidly varying weather patterns and high topographic relief). Empirical approaches include low-pass filtering in time (under the assumption that tropospheric properties are uncorrelated at the multiday timescales sampled by most radars [12] or high-pass filtering in space (for examination of signals with spatial scales that are shorter than the typical length scale of tropospheric variability [13] or errors associated with inaccurate satellite position estimates [14]). These empirical approaches have been shown to be successful in reducing the variability of signals present in single interferograms and time series [15], however, they may also result in the removal of signals of interest [16].

Another empirical approach involves the relationship between phase change and elevation. The tropospheric delay is often modeled as the integral along the path between

Manuscript received April 17, 2020; revised May 18, 2020; accepted June 7, 2020. This work was supported in part by Jet Propulsion Laboratory, California Institute of Technology, under a contract with the National Aeronautics and Space Administration under Grant 80NM0018D004 and in part by JPL Strategic University Research Partnerships (SURP) Program and NASA under Grant NNX16AL20G. *(Corresponding author: Kyle Dennis Murray.)*

Kyle Dennis Murray is with the Department of Earth Sciences, University of Hawaii, Honolulu, HI, USA (e-mail: murray8@hawaii.edu).

Rowena B. Lohman is with the Department of Earth and Atmospheric Sciences, Cornell University, Ithaca, NY 14853 USA (e-mail: rbl62@cornell.edu).

David P. S. Bekaert is with Jet Propulsion Laboratory, California Institute of Technology, Pasadena, CA 91109 USA (e-mail: david.bekaert@jpl.nasa.gov).

This article has supplementary downloadable material available at http://ieeexplore.ieee.org, provided by the authors.

Color versions of one or more of the figures in this article are available online at http://ieeexplore.ieee.org.

Digital Object Identifier 10.1109/TGRS.2020.3003271

0196-2892 © 2020 IEEE. Personal use is permitted, but republication/redistribution requires IEEE permission.
See https://www.ieee.org/publications/rights/index.html for more information.

Authorized licensed use limited to: Cornell University Library. Downloaded on July 01,2020 at 23:41:42 UTC from IEEE Xplore. Restrictions apply.

This article has been accepted for inclusion in a future issue of this journal. Content is final as presented, with the exception of pagination.

the satellite and the ground of the predicted delay due to atmospheric pressure, temperature, and humidity, with several empirical scaling constants [17]. This integrated delay is often highly correlated with elevation and has frequently been used to reduce the impact of tropospheric delays in areas with topographic relief. Both linear and power-law relationships between phase and elevation have been used to mitigate the impact of these delays [18]–[24]. Spatial variability in tropospheric properties, and in their relationship to elevation, can be significant and will result in biases if ignored [25].

Both linear and power-law phase-elevation corrections have limitations. First, as with any empirical approach, removing the phase-elevation dependence can partially or completely remove real deformation signals if the actual deformation is also correlated with elevation. A common example of this is the case of volcanic inflation and deflation signals, which tend to be approximately centered at the volcanic edifice [26]. This problem is typically avoided by excluding the area of suspected deformation during estimation of the phase-elevation dependence—relying on the assumption that lateral variability of tropospheric properties is not significant and that the surrounding topography has sufficient relief to sample the elevation range of interest. Other studies have used a multiscale approach with spatial bandpass filtering to remove targeted deformation signals of known spatial scales [23]. In the work shown here, we address this problem by automatically excluding areas that are characterized by significant deformation with characteristic timescales of several months or longer (Section II-C).

The second major challenge facing empirical methods for removing phase-elevation dependence is that tropospheric properties can vary significantly over the spatial scales sampled by SAR imagery [18], [19], [22], [27]. These variations can be particularly strong, for example, in interferograms that include topographic divides separating coastal regions from inland areas [27]. In some cases, even the sign of the relationship between phase and elevation can change within a single interferogram [19].

Previous studies have addressed the spatial variability by initially segmenting the interferogram into predefined windows and applying the phase-elevation correction separately in each window [18], [22], [25]. Windowing approaches can use a rectangular window with a constant, predefined size [18], [19], [22], [25], or adjust the window size based on local elevation gradients [22]. Bekaert *et al.* [27] developed a segmentation approach based on the predicted behavior of test particles in the presence of topography and the average regional wind field.

In this work, we explore a method for automatic segmentation of the study area based on the data itself. We apply the K-means clustering algorithm to our set of interferograms, which allows us to avoid the need for any *a priori* choice of segmentation styles. We present results from a research area in south-central Mexico (Fig. 1) using this method and compare against some of the standard approaches for mitigating the effects of tropospheric variability. We validate our results with synthetic tests (Section III-B), and compare our corrected time series with GNSS measurements (Fig. 9).

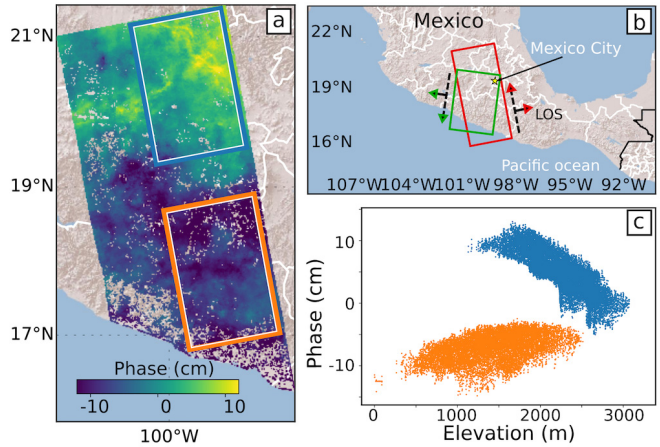

Fig. 1. Example showing phase and elevation variability in two distinct areas for the interferogram pair June 8, 2015-July 2, 2015. (a) Ascending interferogram with blue and orange rectangles encompassing pixels plotted as blue and orange in panel (c). (c) Spatial variability of phase-elevation dependence. (b) Footprints of ascending (red, track 78) and descending (green, track 41) Sentinel-1 tracks used in this study.

II. Data and Methods

A. Test Sites and SAR Data

Our study area covers a large area (∼145 000 km^2) in south-central Mexico (Fig. 1). We use both ascending and descending C-band SAR imagery from the Sentinel-1a/b satellites, part of ESA's Copernicus Program [1], spanning January 2015–August 2018 (Table 3.1 in the Supplementary Material). We generated interferograms using the InSAR Scientific Computing Environment (ISCE, [28] and the associated stack processor [29]). This area of Mexico is of particular interest for studies of crustal deformation due to tectonic [27], [30]–[33], volcanic [34], and anthropogenic deformation [35]. It is also a region with high topographic relief—ranging from sea level to over 4500 m, and where the phase-elevation dependence varies significantly even within individual interferograms (Fig. 2).

Flight direction	**Ascending**	**Descending**
Sentinel-1 Track #	78	41
Resolution	∼300 m	∼200 m
Number of dates	132	125
Date range	11/23/2015 - 9/9/2019	4/30/2015 - 3/16/2019

B. Clustering Algorithm and Correction

K-means clustering [36] is an unsupervised machine-learning algorithm that groups similar data points together to aid in the discovery of underlying patterns. The algorithm can be applied to data with any number of dimensions. The algorithm iteratively estimates cluster centroids through minimization of the sum of the squared distance from each individual data point a given centroid. In each iteration, each data point is assigned to the nearest cluster. This is followed by an update step, in which each cluster centroid is recalculated based on the current set of points assigned to that cluster. The number of clusters, k, must be predefined based on either *a priori* knowledge and/or by a metric such as using the minimum number of clusters that provide the maximum total

Authorized licensed use limited to: Cornell University Library. Downloaded on July 01,2020 at 23:41:42 UTC from IEEE Xplore. Restrictions apply.

This article has been accepted for inclusion in a future issue of this journal. Content is final as presented, with the exception of pagination.

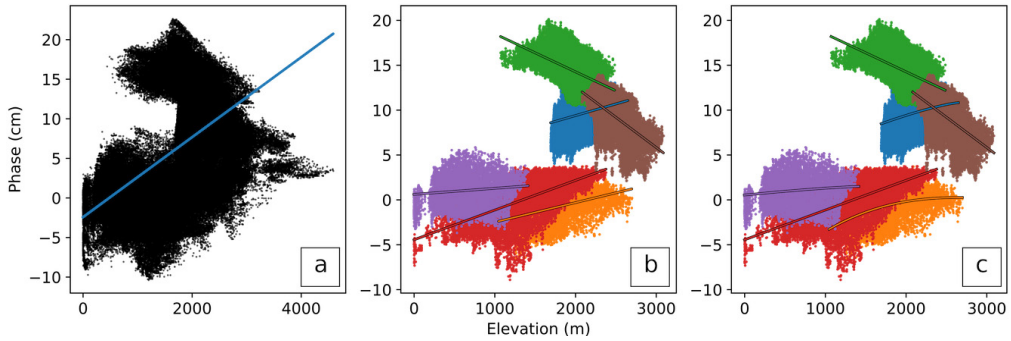

Fig. 2. Elevation versus phase for ascending interferogram June 8, 2015–July 2, 2015 with (a) best linear fit, (b) separate linear fits, and (c) power-law fits to six clusters. We reduce the impact of outliers by removing the points within each cluster that are furthest from the centroid (5% of points for each cluster).

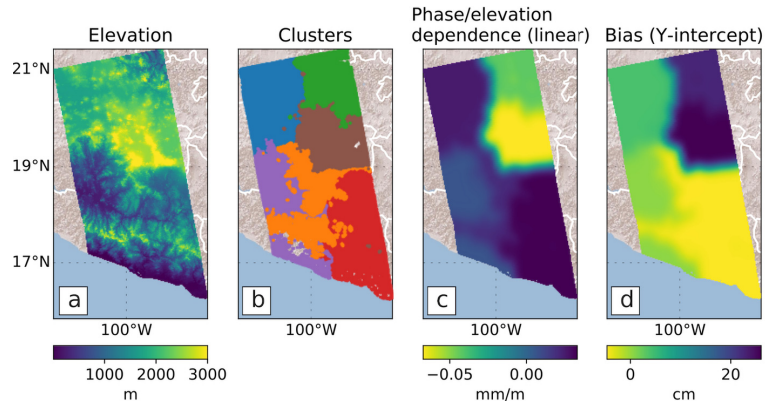

Fig. 3. (a) Elevation map from SRTM-30 DEM, (b) six clusters from Fig. 2(b) and (c) (the same colors) shown in map view for ascending interferogram June 8, 2015–July 2, 2015, and (c) slopes and (d) y-intercepts of the best-fit linear relationship between elevation and phase for each cluster.

reduction of the within-cluster sum of squares or a tradeoff between the resulting fit to the data and number of clusters.

We used the K-means algorithm to identify clusters within the four dimensions of our data: interferometric phase, latitude, longitude, and elevation (Figs. 3 and 4). We initially masked out potentially deforming areas (Section II-C). We applied a whitening transformation to the data prior to clustering to ensure that each dimension contributed equally to the determination of cluster centroids. We select the minimum number of clusters, k, that balanced the total root mean square (rms) reduction of the interferogram [Fig. 5(a)]—similar to the commonly used "L-curve," or "elbow method" [37], [38]. For the data shown here, we find that the use of six clusters significantly improves our result, with limited improvement from the inclusion of additional clusters [Fig. 5(a)]. We removed outliers from each cluster so that any data that was potentially misclassified by the clustering algorithm did not contribute to the estimate of phase-elevation dependence. Outlier removal was done using a one-class support vector machine (SVM) [39], [40] with a radial basis function kernel—an efficient unsupervised algorithm. We removed outliers based on a 5% criterion. Finally, we examined the phase-elevation dependence for each individual cluster of pixels and find both the best-fit linear and power-law fit in a least-squares sense. Although Bekaert *et al.* [19] demonstrated that the power-law relationship is more physically reasonable (e.g., it does not predict large delays at arbitrarily large heights within the troposphere), we include the linear fits as well, for comparison with previous efforts. For the linear relationship [Fig. 2(b)], we use

$$\Delta\phi_{\text{tropo}} = A_{\Delta\phi} h + \Delta\phi_0 \tag{1}$$

where A is the phase-elevation dependence, h is the elevation, and $\Delta\phi_0$ is the phase at zero elevation (y-intercept). For the power-law relationship [Fig. 2(c)], we use

$$\Delta\phi_{\text{tropo}} = A'_{\Delta\phi}(h_0 - h)^{\alpha} \tag{2}$$

where h_0 is the reference height (set to 7000 m in this study [19]) where the differential tropospheric phase converges to zero [19], α is a constant describing the power-law decay, and $A'_{\Delta\phi}$ is the coefficient that relates phase to elevation.

After solving for the linear or power-law parameters for each cluster, we reduce sharp, nonphysical artifacts in the transitions between clusters [Fig. 3(c)] by filtering each parameter (e.g., $A_{\Delta\phi}$ and $\Delta\phi_0$) individually in latitude–longitude space by convolution with a 7×7 km Gaussian kernel. Kernel sizes between 3 and 10 km resulted in the best improvements, but this smoothing step has a minor impact on the correction (Section III-A; Fig. S3 in the Supplementary Material). The result is a spatially variable map of phase-elevation dependence—each pixel in the image has an expected model for how much topography contributes to the phase at that pixel. This model of phase at each pixel in the cluster ($\Delta\phi_{tropo}$) is subtracted from the corresponding pixel in the original interferogram to recover a corrected image. This is simply

Authorized licensed use limited to: Cornell University Library. Downloaded on July 01,2020 at 23:41:42 UTC from IEEE Xplore. Restrictions apply.

This article has been accepted for inclusion in a future issue of this journal. Content is final as presented, with the exception of pagination.

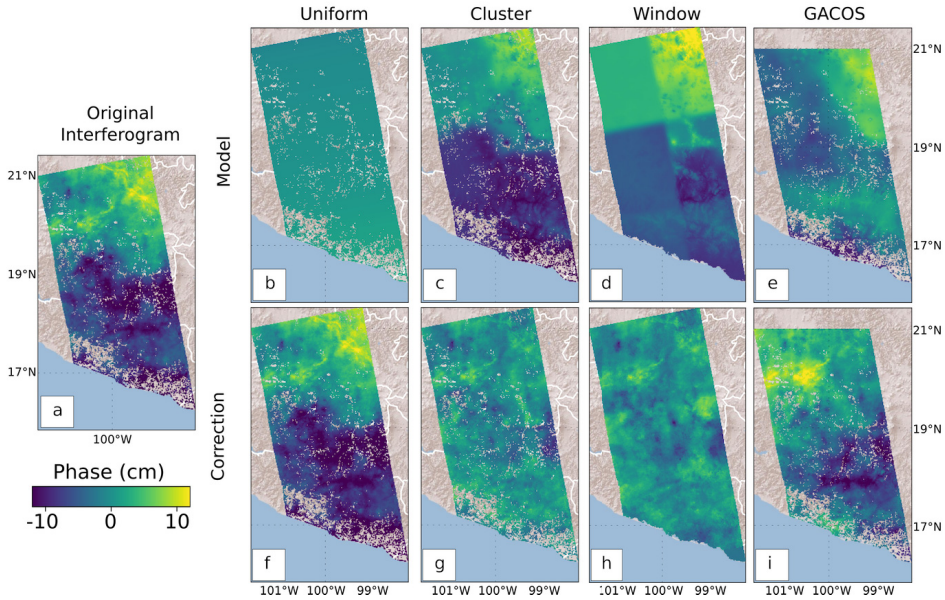

Fig. 4. (a) Ascending interferogram June 8, 2015–July 2, 2015. (b) Tropospheric model of uniform (one cluster) phase-elevation dependence [see Fig. 2(a)]. (c) Cluster power-law phase-elevation model [see Fig. 2(c)]. (d) Six rectangular window phase-elevation model. (e) GACOS model of the tropospheric delay. (f)–(i) Respective corrected interferograms for (b)–(e). All panels shown with the same color range.

written as

$$\Delta\phi_{\text{corrected}} = \Delta\phi_{\text{original}} - \Delta\phi_{\text{tropo}}. \tag{3}$$

To apply this method to a time series, we first invert for an uncorrected displacement time series, mask deforming regions (Section II-C), and perform the cluster analysis on the inferred signal for each individual date. We then examine characteristics of the resulting corrected displacement time series (Section III-C).

C. Masking

As described above, elevation-dependent empirical corrections can also remove deformation signals of interest that also happen to be correlated with elevation. Similarly, large deformation signals can bias the inferred elevation-dependence and result in over- or underprediction of the appropriate elevation-dependence to use in the nondeforming regions. To address this, we analyzed the temporal characteristics of the signal at each pixel. Signals with characteristic timescales greater than a few months are assumed to be potential signals of interest associated with real ground displacements, such as transient or secular tectonic deformation. We identified these areas by applying a temporal low pass filter with a cutoff period of three months to the time series at each pixel and computing the standard deviation of the remaining signal. Pixels with a standard deviation greater than 9 cm over the entire time period were excluded from the phase-elevation dependence calculations. This threshold corresponds to about 0.5 cm of average variation over a three-month time span for our data set. This could include deformation from slow slip, seasonal hydrologic cycles, and/or anthropogenic-related deformation. This is a fairly conservative cutoff, because we expect true deformation time series to not complete a full wavelength within even a one year period. Large (greater than 9 cm) step-like signals such as coseismic offsets should also be captured by this approach. We also excluded pixels exhibiting low coherence or those in areas covered by water. In total, roughly 40% of the pixels were masked before the phase-elevation clustering and analysis, including areas of known subsidence associated with the extraction of groundwater near Mexico City and other

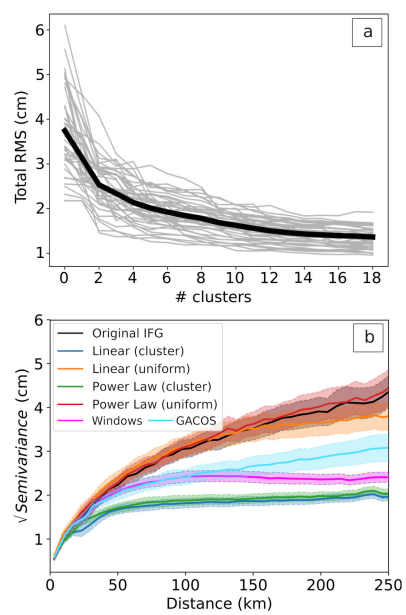

Fig. 5. (a) Total rms for 40 ascending interferograms from south-central Mexico versus the number of K-means clusters used in the correction. Zero clusters corresponds to the original interferogram with no correction applied, and one cluster is equivalent to the uniform phase-elevation dependence correction with no spatial variability. The black line is the mean rms of all 40 interferograms. (b) Averaged semivariogram for 40 interferograms before and after phase-elevation dependence correction with and without cluster analysis. Shaded colored regions indicate 95% confidence, based on the variation within the ensemble of interferograms. The semivariograms from corrected interferograms using the windowing approach and the GACOS model are shown for comparison (pink and light blue).

Authorized licensed use limited to: Cornell University Library. Downloaded on July 01,2020 at 23:41:42 UTC from IEEE Xplore. Restrictions apply.

This article has been accepted for inclusion in a future issue of this journal. Content is final as presented, with the exception of pagination.

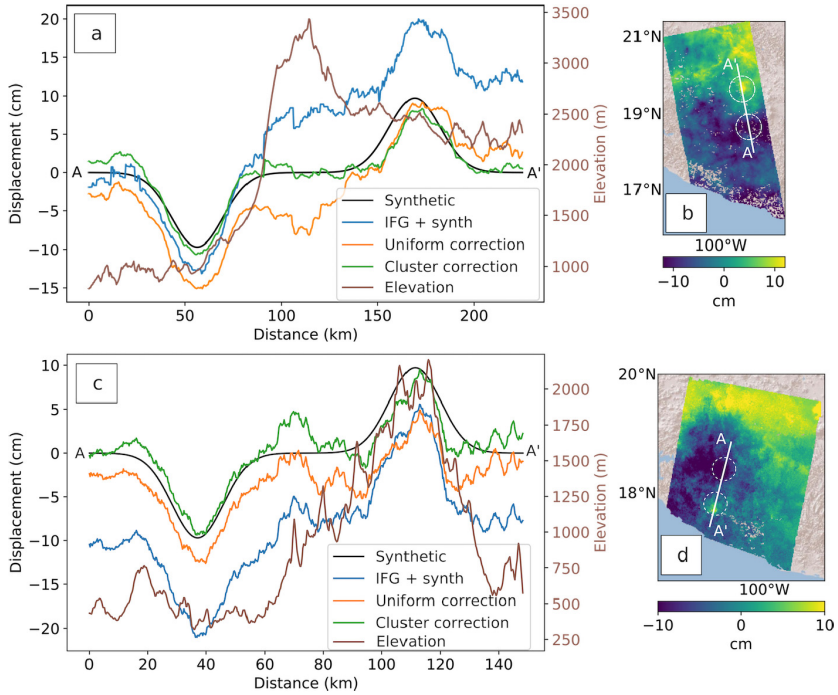

Fig. 6. (a) and (b) Ascending (June 8, 2015–July 2, 2015) and descending (November 8, 2015–March 16, 2019). (c) and (d) Profiles [from white lines in maps (b) and (d)] of negative and positive synthetic Gaussian signals (black line), the synthetic signal added to the ascending interferogram (blue line), the same interferogram after applying a uniform phase-elevation dependence correction (orange line), and the interferogram after applying a six-cluster phase-elevation dependence correction (green line). Elevation across the same profile is also plotted (brown line) with a scale bar on the right y-axis.

metropolitan areas. Areas impacted by sufficiently large abrupt events, such as landslides, or coseismic deformation associated with earthquakes (e.g., the February 16, 2018, M7.2 Pinotepa earthquake, [41] will also be masked by our criterion, but should be masked manually if the timing and location of the signal can be inferred—particularly when the offset is smaller than several cm.

III. Results and Discussion

A. Corrections to Interferograms

In order to evaluate the performance of our approach, we apply our method to a total of 257 nonredundant interferograms covering the two tracks. Interferograms from south-central Mexico have strong atmospheric signals with magnitudes of up to 20 cm within single interferograms [Fig. 1(a)]. The magnitudes and spatial characteristics vary widely throughout time, but are generally correlated with topography. In particular, the phase versus elevation relationship near the coast is often very different from that observed in inland areas—a contrast that can also be observed between the areas of lower topography in the west versus higher topography in the east. The phase-elevation dependence for the interferogram spanning June 8, 2015–July 2, 2015 [Figs. 1(a) and 2] illustrates a clear example where even the sign of this relationship changes within the image, and where a standard "one-cluster" correction approach is ineffective [Figs. 2(a) and 4(d)].

After making the interferograms we perform cluster analysis and solve for, and remove, the phase-elevation dependence from each cluster. Results for the example interferogram from Fig. 1 are shown in Fig. 2(b) and (c) with the map view extent of the clusters indicated in Fig. 3. The results of correcting this interferogram with a power-law relationship for one cluster (uniform correction) versus six clusters are shown in Fig. 4. Cluster boundaries tend to be associated with sharp changes in relief, such as mountain ridges or valley margins. In the area of interest, the key boundaries include the coastal mountain range, a large inland basin, a high inland plateau, and a lower basin leading into Mexico City. As mentioned above, we find that there is generally little additional reduction of rms from the original interferograms to the corrected interferograms using more than six clusters [Fig. 5(a)]. Additional, smaller clusters also are associated with challenges, such as a lack of sufficient variation in elevation within a given cluster in order to reliably estimate the phase-elevation correlation, or overfitting of tropospheric turbulence, which does not correlate reliably with elevation. Strong gradients in pressure, temperature, and/or water vapor can sometimes result in cluster boundaries that are not associated with features in the terrain, but this appears to occur infrequently. We tested the correction with varying kernel sizes for the spatial smoothing step to reduce sharp transitions between clusters. In general, we found only slight improvements to the resulting correction with kernel sizes greater than $\sim$3 km^2 (Fig. S3 in the Supplementary Material). Furthermore, the use of smoothing kernel sizes greater than $\sim$10 km^2 added no additional impact (Fig. S3 in the Supplementary Material).

Characterization of the efficacy of any tropospheric correction approach can be performed by inspecting the statistics of the residual after correction in a range of ways, including the reduction in rms, frequency domain analysis, or semivariograms [11]. The reduction in rms is a useful metric for characterizing the overall reduction of signal at all spatial scales, and is approximately equivalent to the

Authorized licensed use limited to: Cornell University Library. Downloaded on July 01,2020 at 23:41:42 UTC from IEEE Xplore. Restrictions apply.

This article has been accepted for inclusion in a future issue of this journal. Content is final as presented, with the exception of pagination.

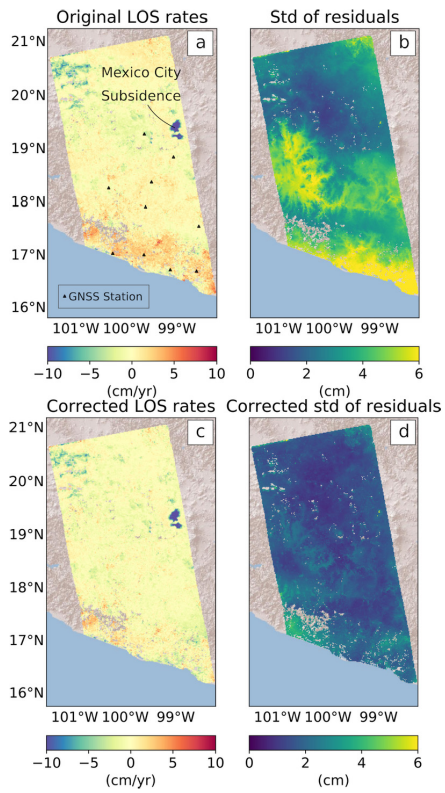

Fig. 7. Average linear rate maps with respect to mean of nondeforming areas (a) before and (c) after phase-elevation dependence correction for ascending path. Standard deviation of residual from linear rate at to each pixel (b) before and (d) after phase-elevation dependence correction. Time series consists of 104 dates spanning the time range November 23, 2015–March 19, 2019 with no redundant interferometric pairs. Black triangles in (a) correspond to GPS stations in Fig. 8.

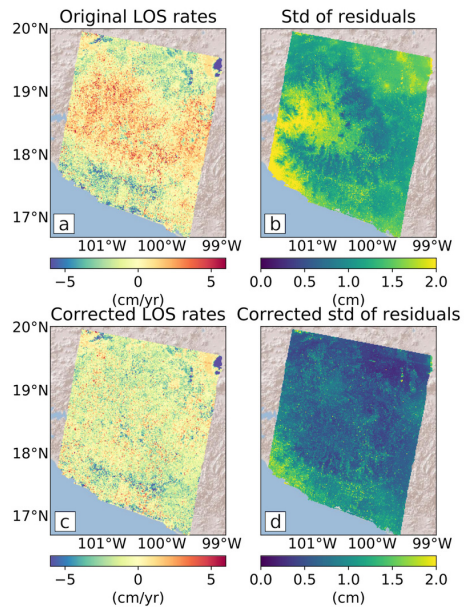

Fig. 8. Average linear rate maps (a) before and (c) after phase-elevation dependence correction for descending path. Standard deviation of residual from linear rate at to each pixel (b) before and (d) after phase-elevation dependence correction. Rate map was computed with a subset of 56 interferograms spanning the time range November 8, 2015–March 16, 2019 with no redundant pairs to approximate the time span of the ascending track for comparison.

square root of the semivariogram's sill. Therefore, in this text we convey the overall efficacy of the correction technique based on the reduction of rms, however it is important to consider how well the correction performs at a range of spatial scales—which is best observed in the semivariogram [Fig. 5(b)] [11]. Average total semivariance decreases from ∼4 cm to ∼1.8 cm after applying the power-law correction on six clusters [Fig. 5(b)] for a sample of 40 ascending interferograms. Uniform (single cluster) corrections perform poorly in this study area, with insignificant improvement in average rms or the semivariogram [Fig. 5(b)]. Power-law models and linear models perform equally well, according to the rms and semivariogram metrics alone. We do not expect to reduce the impact of turbulent tropospheric variations over relatively short spatial scales of ∼25 km or less [Figs. 4(c) and 5(b)]. Results show that the signals at larger wavelengths are greatly reduced [Figs. 4 and 5(b)]. Aside from turbulent tropospheric effects, much of the remaining signal may be attributed to ionospheric variations and any other tropospheric variations that deviate from the phase-elevation dependence found within clusters, as well as any other sources of noise or real deformation.

We also compare the clustering approach with results from a windowing approach (Fig. S.2 in the Supplementary Material) as well as the tropospheric delay product from Generic Atmospheric Correction Online Service (GACOS) for InSAR [42]. The windowing approach consisted of separating the interferogram into six rectangular windows (to match the number of clusters) (Fig. S.2 in the Supplementary Material). We then computed the phase-elevation dependence within each rectangle the same way we did for each cluster (Section II). We found this approach improves upon the uniform phase-elevation correction, but the clustering algorithm results in significantly greater reduction in the semivariance at most spatial scales.

B. Synthetic Tests

As discussed above, empirical tropospheric corrections can result in partial removal of the true deformation signal if it also correlated with elevation. To avoid this, as described in Section II-C, we apply a mask to any known or potentially deforming areas prior to applying the correction. Although masking is quite effective when the signal is known or large enough to be masked out by the criteria described above, there will likely be cases in which identifying real deformation a priori is challenging—particularly when the deformation only spans a short time span. Thus, we explore a worst case scenario in which a synthetic "real" deformation signal is present in a single interferogram to test how well the signal is preserved after applying the correction. To do this, we introduced two synthetic deformation signals into example ascending (June 8, 2015–July 2, 2015) and descending synthetic signals consisted of adjacent positive and negative 2-D Gaussians, each spanning approximately 75 km at 2-sigma (Fig. 6) with peak amplitudes of 10 cm. In an ideal case, the removal of our inferred tropospheric model would not change the size or shape of the input synthetic

Authorized licensed use limited to: Cornell University Library. Downloaded on July 01,2020 at 23:41:42 UTC from IEEE Xplore. Restrictions apply.

This article has been accepted for inclusion in a future issue of this journal. Content is final as presented, with the exception of pagination.

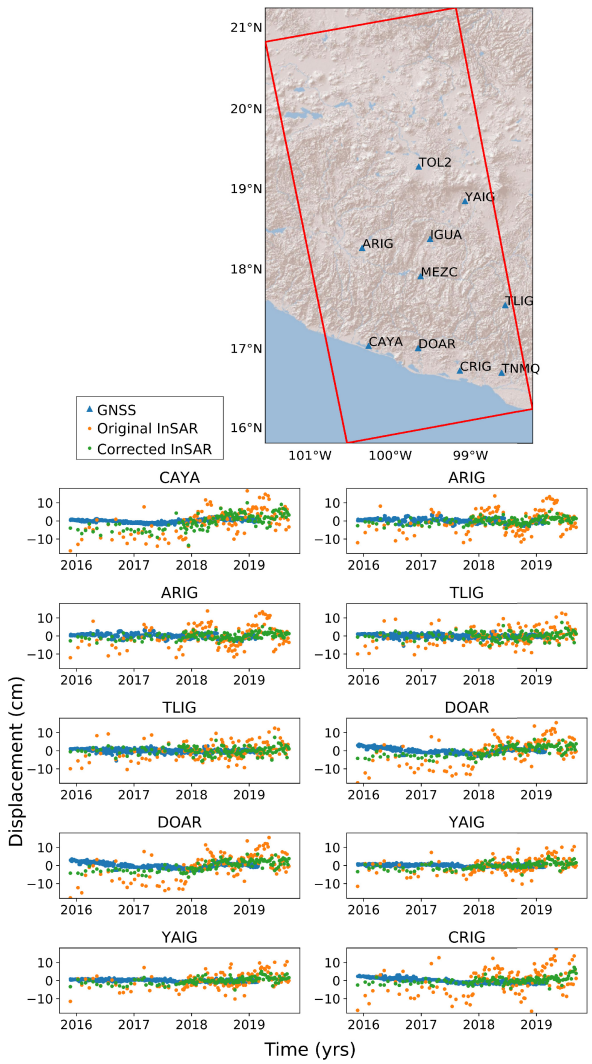

Fig. 9. Comparisons of time series at locations of GNSS stations (locations shown in left, InSAR footprint in red). GNSS measurements (blue triangles) are plotted with the original (orange), and corrected (green) InSAR measurements. Mean value was removed from each time series for comparison.

signals. We examine the impact of both linear and power-law phase-elevation dependence corrections using six clusters and a uniform correction. The synthetic signal [black curve, Fig. 6(a) and (c)] is generally well preserved after applying our correction in both the ascending and descending data sets. Note that in both examples (Fig. 6), one of the signals correlates strongly with elevation along the profile. If the clusters chosen by our algorithm were too small, the inferred phase-elevation dependence would be heavily impacted by the synthetic signal. In our synthetic tests, the clusters are still large enough, and sample a large enough range of relief, that the inferred tropospheric correction for the clusters does not significantly reduce the input synthetic signal.

C. Time Series Results

For each track, we compare the characteristics of the best-fit average linear deformation rate (i.e., the secular trend) at each pixel. We illustrate these results in map view (Figs. 7 and 8) and at selected points (Fig. 9). The spatial variability of the average linear rates was reduced after applying the phase-elevation dependence correction, and the average standard deviation of linear rate residuals decreases from approximately 3 to 1.5 cm [Figs. 7(b) and (d)] for the ascending track, and approximately 1.5–0.5 cm for the descending track [Figs. 8(b) and (d)].

IV. Conclusion

We presented a technique for characterizing the topography-correlated, and long-wavelength, tropospheric noise in InSAR imagery using a spatially variable, cluster-based, empirical model of the dependence of phase on elevation. We outline a method to automatically mask potential real deformation through temporal filtering before computing the phase-elevation dependence using cluster analysis. This approach is a significant improvement over uniform phase-elevation corrections, particularly when the interferograms cover a large area and contain regions with distinct weather patterns and microclimates. The total rms averaged over 131 sequential interferograms for the ascending track was decreased by ∼50% after applying the correction, with the greatest effect on spatial scales greater than ∼25 km. We also demonstrated that this method allows us to recover a synthetic signal introduced to the interferograms, even when there is some correlation between the synthetic signal and elevation. Uncertainties for long-term averaged linear rate estimates were reduced from 0.94 to 0.63 cm/yr (averaged over the area of the ascending track). With the overwhelming expansion of SAR data that is likely to come with the continued operation of existing satellites and the launch of future missions, such as NISAR, this approach supports the development of effective, semiautomatic processing methods that can reduce the impact of tropospheric noise on the resulting InSAR time series.

Acknowledgment

Copernicus Sentinel-1 SAR imagery used in this study is from the European Space Agency (ESA), downloaded through the Alaska Satellite Facility (ASF) at https://vertex.daac.asf.alaska.edu. The authors thank the Jet Propulsion Laboratory for providing us with ISCE (Rosen *et al.*, 2012), the stack processing capability [29], and the SRTM topographic data [42]. GNSS data are obtained from the Servicio Sismologico Nacional (SSN) GNSS Network and Trans-boundary Land and Atmosphere Long-term Observational and Collaborative Network (TLALOCNet) and Instituto Nacional de Estadistica e Informacion (INEGI). They thank Servicio Sismológico Nacional (Xyoli Perez-Campos and Hugo Melendez), UNAVCO and INEGI for GNSS RINEX data files. Javier-Alejandro Gonzalez-Ortega did processing of the raw GNSS data. The raw data was processed using GAMIT/GLOBK v10.7 software [43]. Finally, the authors thank the editor and two anonymous reviewers for their helpful critical comments.

References

[1] F. De Zan and A. Monti Guarnieri, "TOPSAR: Terrain observation by progressive scans," *IEEE Trans. Geosci. Remote Sens.*, vol. 44, no. 9, pp. 2352–2360, Sep. 2006.

[2] H. Berrada Baby, P. Golé, and J. Lavergnat, "A model for the tropospheric excess path length of radio waves from surface meteorological measurements," *Radio Sci.*, vol. 23, no. 6, pp. 1023–1038, Nov. 1988.

Authorized licensed use limited to: Cornell University Library. Downloaded on July 01,2020 at 23:41:42 UTC from IEEE Xplore. Restrictions apply.

This article has been accepted for inclusion in a future issue of this journal. Content is final as presented, with the exception of pagination.

[3] M. Bevis, S. Businger, T. A. Herring, C. Rocken, R. A. Anthes, and R. H. Ware, "GPS meteorology: Remote sensing of atmospheric water vapor using the global positioning system," *J. Geophys. Res.*, vol. 97, no. D14, pp. 15787–15801, Oct. 1992.

[4] R. Hanssen and R. Bamler, "Evaluation of interpolation kernels for SAR interferometry," *IEEE Trans. Geosci. Remote Sens.*, vol. 37, no. 1, pp. 318–321, Jan. 1999.

[5] E. Tymofyeyeva and Y. Fialko, "Mitigation of atmospheric phase delays in InSAR data, with application to the Eastern California shear zone," *J. Geophys. Res., Solid Earth*, vol. 120, no. 8, pp. 5952–5963, Aug. 2015.

[6] H. A. Zebker, P. A. Rosen, and S. Hensley, "Atmospheric effects in interferometric synthetic aperture radar surface deformation and topographic maps," *J. Geophys. Res., Solid Earth*, vol. 102, no. B4, pp. 7547–7563, Apr. 1997.

[7] M.-P. Doin, C. Lasserre, G. Peltzer, O. Cavalié, and C. Doubre, "Corrections of stratified tropospheric delays in SAR interferometry: Validation with global atmospheric models," *J. Appl. Geophys.*, vol. 69, no. 1, pp. 35–50, Sep. 2009.

[8] Z. Li, E. J. Fielding, P. Cross, and R. Preusker, "Advanced InSAR atmospheric correction: MERIS/MODIS combination and stacked water vapour models," *Int. J. Remote Sens.*, vol. 30, no. 13, pp. 3343–3363, Jul. 2009.

[9] D. P. S. Bekaert, R. J. Walters, T. J. Wright, A. J. Hooper, and D. J. Parker, "Statistical comparison of InSAR tropospheric correction techniques," *Remote Sens. Environ.*, vol. 170, pp. 40–47, Dec. 2015.

[10] Z. Li, "Comparison of precipitable water vapor derived from radiosonde, GPS, and moderate-resolution imaging spectroradiometer measurements," *J. Geophys. Res.*, vol. 108, no. D20, pp. 10-1–10-12, 2003.

[11] K. D. Murray, D. P. S. Bekaert, and R. B. Lohman, "Tropospheric corrections for InSAR: Statistical assessments and applications to the Central United States and Mexico," *Remote Sens. Environ.*, vol. 232, Oct. 2019, Art. no. 111326. [Online]. Available: http://www.sciencedirect.com/science/article/pii/S0034425719303451

[12] T. R. Emardson, M. Simons, and F. H. Webb, "Neutral atmospheric delay in interferometric synthetic aperture radar applications: Statistical description and mitigation," *J. Geophys. Res., Solid Earth*, vol. 108, pp. 4-1–4-8, no. B5, May 2003.

[13] S. Williams, Y. Bock, and P. Fang, "Integrated satellite interferometry: Tropospheric noise, GPS estimates and implications for interferometric synthetic aperture radar products," *J. Geophys. Res., Solid Earth*, vol. 103, no. B11, pp. 27051–27067, Nov. 1998.

[14] D. Massonnet and K. L. Feigl, "Radar interferometry and its application to changes in the Earth's surface," *Rev. Geophys.*, vol. 36, no. 4, pp. 441–500, Nov. 1998.

[15] M. E. Pritchard and M. Simons, "A satellite geodetic survey of large-scale deformation of volcanic centres in the Central Andes," *Nature*, vol. 418, no. 6894, pp. 167–171, Jul. 2002.

[16] J. Biggs, T. Wright, Z. Lu, and B. Parsons, "Multi-interferogram method for measuring interseismic deformation: Denali fault, Alaska," *Geophys. J. Int.*, vol. 170, no. 3, pp. 1165–1179, Sep. 2007.

[17] R. F. Hanssen, *Radar Interferometry: Data Interpretation and Error Analysis*, vol. 2. Cham, Switzerland: Springer, 2001.

[18] M. Béjar-Pizarro, A. Socquet, R. Armijo, D. Carrizo, J. Genrich, and M. Simons, "Andean structural control on interseismic coupling in the North Chile subduction zone," *Nature Geosci.*, vol. 6, no. 6, pp. 462–467, Jun. 2013.

[19] D. P. S. Bekaert, A. Hooper, and T. J. Wright, "A spatially variable power law tropospheric correction technique for InSAR data," *J. Geophys. Res., Solid Earth*, vol. 120, no. 2, pp. 1345–1356, Feb. 2015.

[20] O. Cavalié *et al.*, "Measurement of interseismic strain across the Haiyuan Fault (Gansu, China), by InSAR," *Earth Planet. Sci. Lett.*, vol. 275, nos. 3–4, pp. 246–257, Nov. 2008.

[21] J. R. Elliott, J. Biggs, B. Parsons, and T. J. Wright, "InSAR slip rate determination on the Altyn Tagh Fault, Northern Tibet, in the presence of topographically correlated atmospheric delays," *Geophys. Res. Lett.*, vol. 35, no. 12, pp. 1–5, Jun. 2008.

[22] H. Liang, L. Zhang, X. Ding, Z. Lu, and X. Li, "Toward mitigating stratified tropospheric delays in multitemporal InSAR: A quadtree aided joint model," *IEEE Trans. Geosci. Remote Sens.*, vol. 57, no. 1, pp. 291–303, Jan. 2019.

[23] Y.-N.-N. Lin, M. Simons, E. A. Hetland, P. Muse, and C. DiCaprio, "A multiscale approach to estimating topographically correlated propagation delays in radar interferograms," *Geochem. Geophys. Geosyst.*, vol. 11, no. 9, pp. 1–17, Sep. 2010.

[24] D. Remy, S. Bonvalot, P. Briole, and M. Murakami, "Accurate measurements of tropospheric effects in volcanic areas from SAR interferometry data: Application to sakurajima volcano (Japan)," *Earth Planet. Sci. Lett.*, vol. 213, nos. 3–4, pp. 299–310, Aug. 2003.

[25] C. P. Scott and R. B. Lohman, "Sensitivity of earthquake source inversions to atmospheric noise and corrections of InSAR data," *J. Geophys. Res., Solid Earth*, vol. 121, no. 5, pp. 4031–4044, May 2016.

[26] F. Delgado, M. E. Pritchard, S. Ebmeier, P. González, and L. Lara, "Recent unrest (2002-2015) imaged by space geodesy at the highest risk Chilean volcanoes: Villarrica, Llaima, and Calbuco (Southern Andes)," *J. Volcanology Geothermal Res.*, vol. 344, pp. 270–288, Sep. 2017.

[27] D. P. S. Bekaert, A. Hooper, and T. J. Wright, "Reassessing the 2006 Guerrero slow-slip event, Mexico: Implications for large earthquakes in the Guerrero gap," *J. Geophys. Res., Solid Earth*, vol. 120, no. 2, pp. 1357–1375, Feb. 2015.

[28] P. A. Rosen, E. Gurrola, G. F. Sacco, and H. Zebker, "The InSAR scientific computing environment," in *Proc. 9th Eur. Conf. Synth. Aperture Radar (EUSAR)*, 2012, pp. 730–733.

[29] H. Fattahi, P. Agram, and M. Simons, "A network-based enhanced spectral diversity approach for TOPS time-series analysis," *IEEE Trans. Geosci. Remote Sens.*, vol. 55, no. 2, pp. 777–786, Feb. 2017.

[30] O. Cavalié *et al.*, "Slow slip event in the Mexican subduction zone: Evidence of shallower slip in the Guerrero seismic gap for the 2006 event revealed by the joint inversion of InSAR and GPS data," *Earth Planet. Sci. Lett.*, vol. 367, pp. 52–60, Apr. 2013.

[31] V. Kostoglodov *et al.*, "The 2006 slow slip event and nonvolcanic tremor in the Mexican subduction zone," *Geophys. Res. Lett.*, vol. 37, no. 24, pp. 1–5, Dec. 2010.

[32] K. M. Larson, V. Kostoglodov, S. Miyazaki, and J. A. S. Santiago, "The 2006 aseismic slow slip event in Guerrero, Mexico: New results from GPS," *Geophys. Res. Lett.*, vol. 34, no. 13, Jul. 2007.

[33] M. Vergnolle *et al.*, "Slow slip events in Mexico revised from the processing of 11 year GPS observations," *J. Geophys. Res.*, vol. 115, no. B8, pp. 1–18, 2010.

[34] E. Chaussard, F. Amelung, and Y. Aoki, "Characterization of open and closed volcanic systems in Indonesia and Mexico using InSAR time series," *J. Geophys. Res., Solid Earth*, vol. 118, no. 8, pp. 3957–3969, Aug. 2013.

[35] E. Chaussard, S. Wdowinski, E. Cabral-Cano, and F. Amelung, "Land subsidence in central Mexico detected by ALOS InSAR time-series," *Remote Sens. Environ.*, vol. 140, pp. 94–106, Jan. 2014.

[36] J. MacQueen, "Some methods for classification and analysis of multivariate observations," in *Proc. 5th Berkeley Symp. Math. Statist. Probab.*, vol. 1, Oakland, CA, USA, 1967, pp. 281–297.

[37] T. M. Kodinariya and P. R. Makwana, "Review on determining number of cluster in K-means clustering," *Int. J.*, vol. 1, no. 6, pp. 90–95, 2013.

[38] W. Menke, *Geophysical Data Analysis: Discrete Inverse Theory*. New York, NY, USA: Academic, 2018.

[39] F. Pedregosa *et al.*, "Scikit-learn: Machine learning in Python," *J. Mach. Learn. Res.*, vol. 12, pp. 2825–2830, Oct. 2011.

[40] B. Schölkopf, J. C. Platt, J. Shawe-Taylor, A. J. Smola, and R. C. Williamson, "Estimating the support of a high-dimensional distribution," *Neural Comput.*, vol. 13, no. 7, pp. 1443–1471, Jul. 2001.

[41] S. Tung, E. J. Fielding, D. P. S. Bekaert, and T. Masterlark, "Rapid geodetic analysis of subduction zone earthquakes leveraging a 3-D elastic Green's function library," *Geophys. Res. Lett.*, vol. 46, no. 5, pp. 2475–2483, Mar. 2019.

[42] C. Yu, Z. Li, N. T. Penna, and P. Crippa, "Generic atmospheric correction model for interferometric synthetic aperture radar observations," *J. Geophys. Res., Solid Earth*, vol. 123, no. 10, pp. 9202–9222, Oct. 2018.

Kyle Dennis Murray received the B.S. degree in geology from Montana State University, Bozeman, MT, USA, in 2011, the M.S. degree in geophysics from New Mexico Tech, Socorro, NM, USA, in 2015, and the Ph.D. degree in geophysics from Cornell University, Ithaca, NY, USA, in May 2020.

He is a National Science Foundation GeoPRISMS Post-Doctoral Scholar at the University of Hawaii at Manoa, Honolulu, HI, USA. His research interests include development and applications of space-based geodetic techniques for characterizing crustal deformation related to tectonics and anthropogenic activity.

Authorized licensed use limited to: Cornell University Library. Downloaded on July 01,2020 at 23:41:42 UTC from IEEE Xplore. Restrictions apply.

This article has been accepted for inclusion in a future issue of this journal. Content is final as presented, with the exception of pagination.

Rowena B. Lohman received the B.S. degree in geology and the Ph.D. degree in geophysics from the California Institute of Technology, Pasadena, CA, USA, in 1998 and 2004, respectively.

From 2004 to 2006, she was a Post-Doctoral Scholar with Woods Hole Oceanographic Institute, Woods Hole, MA, USA, and from 2006 to 2007, she was a Post-Doctoral Scholar with Jet Propulsion Laboratory, Pasadena. Since 2015, she has been an Associate Professor with Earth and Atmospheric Sciences Department, Cornell University, Ithaca, NY, USA. Her research interest includes the application of geodesy, including satellite-based interferometric synthetic aperture radar to the study of fault systems and land surface change.

Dr. Lohman was a recipient of the Geodesy Section Award from the American Geophysical Union in 2013.

David P. S. Bekaert received the B.S. and M.S. degrees in aerospace engineering from the Delft University of Technology, Delft, The Netherlands, in 2008 and 2011, respectively, and the Ph.D. degree in geodesy and geophysics from the University of Leeds, Leeds, U.K., in 2015.

From 2011 to 2012, he was a Young Graduate Trainee at the European Space Agency, The Netherlands, and from 2015 to 2016, he was a Caltech Post-Doctoral Scholar at Jet Propulsion Laboratory, Pasadena CA, USA. Since 2016, he has been a Radar Scientist with Radar Science Group, Radar Science and Engineering Section, Jet Propulsion Laboratory. In 2019, he became the Project Scientist for the Advanced Rapid Imaging and Analysis (ARIA) Project for Natural Hazards. His research interest includes application of interferometric synthetic aperture radar (InSAR) processing techniques with earth science and geoscience applications including natural hazards, subsidence, and critical infrastructure monitoring

Authorized licensed use limited to: Cornell University Library. Downloaded on July 01,2020 at 23:41:42 UTC from IEEE Xplore. Restrictions apply.